

# Low Cycle Fatigue Behavior and Microstructural Evolution of Nickel-based Superalloy M951G at Elevated Temperatures

Luqing Cui, Jinlai Liu, Ru Lin Peng, Jinjiang Yu, Johan Moverare and Xiaofeng Sun

The self-archived postprint version of this journal article is available at Linköping University Institutional Repository (DiVA):

<http://urn.kb.se/resolve?urn=urn:nbn:se:liu:diva-166002>

N.B.: When citing this work, cite the original publication.

Cui, L., Liu, J., Peng, Ru L., Yu, J., Moverare, J., Sun, X., (2020), Low Cycle Fatigue Behavior and Microstructural Evolution of Nickel-based Superalloy M951G at Elevated Temperatures, *Materials Characterization*, 163, 110241. <https://doi.org/10.1016/j.matchar.2020.110241>

Original publication available at:

<https://doi.org/10.1016/j.matchar.2020.110241>

Copyright: Elsevier

<http://www.elsevier.com/>



# Low cycle fatigue behavior and microstructural evolution of nickel-based superalloy M951G at elevated temperatures

Luqing Cui <sup>a,b,c</sup>, Jinlai Liu <sup>a</sup>, Ru Lin Peng <sup>c</sup>, Jinjiang Yu <sup>a,\*</sup>, Johan Moverare <sup>c,\*\*</sup>, Xiaofeng Sun <sup>a</sup>

<sup>a</sup> Institute of Metal Research, Chinese Academy of Sciences, Shenyang 110016, China

<sup>b</sup> School of Materials Science and Engineering, University of Science and Technology of China, Hefei 230026, China

<sup>c</sup> Division of Engineering materials, Department of Management and Engineering, Linköping University, Linköping SE-58183, Sweden

**ABSTRACT:** Low cycle fatigue (LCF) tests of the newly developed nickel-based superalloy M951G have been conducted at 900 and 1000 °C under different total strain amplitudes. Results show that the fatigue properties, fracture mechanisms as well as coarsening of  $\gamma'$  precipitates are dependent on testing temperatures and strain amplitudes. Fatigue life and cyclic stress response under the same total strain amplitude at 1000 °C are lower than that at 900 °C, which is due to the degradation of microstructures, shearing of  $\gamma'$  precipitates by dislocations and serious oxidation. Fracture modes change from intergranular cracking to the mixed mode cracking as the strain amplitude increases. At low strain amplitudes, M951G alloy fails in the form of intergranular cracking owing to the oxidation of surface carbides and the relatively low deformation rate. At higher strain amplitudes, the strain localization in grain interior, the distribution of broken carbides and eutectics as well as the relatively higher strain rate are the main reasons for the formation of transgranular microcracks. Ultimately, the effects of fatigue conditions on coarsening of cubic  $\gamma'$  precipitates are also analyzed from the aspect of  $\gamma'$  volume fraction, fatigue life and flow stress difference between the  $\gamma/\gamma'$  interfaces.

\*Corresponding author.

\*\*Corresponding author.

E-mail: jjyu@imr.ac.cn (Jinjiang Yu), johan.moverare@liu.se (Johan Moverare).

**Keywords:** M951G alloy; Low cycle fatigue; Fatigue life; Cyclic stress amplitude; Fracture modes; Coarsening of  $\gamma'$  precipitates

## 1. Introduction

As unique high temperature materials used in the aircraft engines and industry gas turbine engines, nickel-based superalloys consist of plenty of ordered  $\gamma'$  precipitates with  $L1_2$  structure coherently embedded in  $\gamma$  matrix with fcc (face-centered cubic) structure, thus displaying excellent resistance to mechanical and chemical degradation at temperatures close to their melting points [1-7].

During actual service, the hot section components of engines are exposed to the interactions of temperature and stress, which finally results in the failure of the superalloys. Therefore, it is necessary to study the influences of temperature and stress on the mechanical properties of superalloys. In the past several decades, much work has been done in this field, such as tensile [8-14] and creep deformations [5, 7, 15-20] of superalloys. However, in practical application, the blades are subjected to cyclic thermal stress resulting from start-up and shut-down procedures [21, 22]. In addition, the fatigue fracture is the main mode of blades failure, especially the low cycle fatigue (LCF). It has become one of the major considerations for engineers to evaluate the security and reliability of a newly designed superalloy [23]. Therefore, LCF deformation can approach the actual application conditions of turbine engine blades under service and more attention should be paid on it.

In the previous work, the effects of testing temperature [24-26], loading waveform [27], thermal gradient [28-31], strain amplitude [32-34] and frequency [35, 36] have been widely investigated on the LCF behaviors of superalloys. Among these influencing factors, testing

temperature and strain amplitude are of special interest [4, 33, 37-42]. Chu studied the LCF behavior of DZ951 alloy at a temperature range from 700 to 900 °C. Their results showed that the fatigue life of DZ951 alloy did not monotonously decrease with the increase of temperature, but had a strong dependence on the total strain amplitude [43]. At the low temperature of 700 °C, the fatigue failure of DZ951 alloy was mainly due to the cyclic plastic deformation process; while the failure mostly resulted from the combined effects of fatigue and creep damage with the total strain amplitude ranging from 0.6 to 1.2% at the high temperature of 900 °C [43]. Research from Dewa demonstrated that with an increasing total strain amplitude the fatigue tests showed a decrease in fatigue resistance [44]. It was due to the activation of the slip system and an increase in plastic deformation [44]. In addition, the effects of temperature on the dislocation and slip band motion were also investigated [39, 45, 46]. Slip bands were the main slip characteristics at 500 and 750 °C. However, the extension of intrusion and extrusion became weak as the testing temperature increases [47].

Since precipitation strengthening is the most important strengthening method for nickel-based superalloys, the size of the  $\gamma'$  phase is an important parameter for fatigue properties of the superalloys [6, 43, 48-51]. In the previous studies, extensively discussions were focused on the variation of  $\gamma'$  precipitate size during fatigue tests [6, 43, 48-50]. Li studied the effect of Re on the  $\gamma'$  precipitates size of a second-generation single-crystal superalloy during low cycle fatigue deformation [48], results show that the addition of Re suppresses the growth of the  $\gamma'$  phase by decreasing the rate of elemental diffusion. In addition, the effects of temperature on the  $\gamma'$  precipitate size were also discussed. Research from Antolovich et al. [50] demonstrated that particle coarsening occurred in Rene 80 after LCF deformations at 871 and 982 °C, which

resulted in the loss of coherency between  $\gamma$  and  $\gamma'$  phases. However, the  $\gamma'$  precipitates in the DZ951 alloy did not coarsen during the LCF test at 900 ° C, but the morphology of them changed from cubic to spherical [43]. Apart from that, the relationship between crystal orientations and precipitate dimensions has also been studied during LCF deformations [49, 52]. Result showed that crystal orientation has little effect on the size of the  $\gamma'$  precipitates. Whether the orientation is [001], [011] or [111], the  $\gamma'$  precipitate gradually coarsens and spheroidizes as the strain amplitude decreases [49].

As mentioned above, although extensive investigations have been performed, the effects of testing temperature and total strain amplitude on the fatigue life, cyclic stress response and fracture mechanisms of superalloys are still not completely clear, especially for polycrystalline superalloys at elevated temperatures. And making it clear is of great significance for a better understanding of LCF behaviors for superalloys. On the other hand, the relationship between fatigue conditions and precipitate dimensions is also still unclear. Therefore, in the present work, the new nickel-based superalloy M951G [53] was selected as the experimental alloy to study the relationship between fatigue conditions and coarsening of  $\gamma'$  precipitates.

## **2. Materials and experimental procedures**

M951G is designed by the Institute of Metal Research (IMR), Chinese Academy of Sciences for use in gas turbines and aero engines. The nominal chemical composition of this material is listed in Table1. The master alloy was remelted in a vacuum induction furnace, with the mold preheating and pouring temperatures set at 900 and 1450 °C, respectively. The procedures of heat treatment conducted on the as-cast alloy were as follows: 1210 °C×4 h, AC→1100 °C×4 h, AC→870 °C×24 h, AC (AC: air cooling).

Fig. 1a shows the typical morphologies of  $\gamma'$  precipitates after heat-treatment. According to the configurations of  $\gamma'$  phase, it can be divided into two types. One is the cubic  $\gamma'$  phase, the size of which is uniform to a high degree. The other is spherical  $\gamma'$  phase distributed in  $\gamma$  channels between cubic  $\gamma'$  precipitates. Fig. 1b and c show the dislocation configurations of M951G alloy in the heat-treated microstructure. Isolated misfit dislocations along the  $\gamma/\gamma'$  interfaces are occasionally observed, as displayed in Fig. 1c. The dislocation morphology in Fig. 1c represents the typical structure for most regions of the heat-treated material. However, regions of “zig-zag” dislocations in Fig. 1b can be also occasionally seen in M951G alloy. The schematic illustration of zig-zag dislocations is shown in Fig. 1d, which are due to the cross-slip of  $1/2\langle 101 \rangle$  leading screw segments on  $\{111\}$  planes and leaving  $60^\circ$  mixed dislocations at the horizontal upper and bottom surfaces of the  $\gamma'$  precipitates [47].

LCF specimens with a gauge length of 16 mm and a diameter of 6.5 mm were machined from heat-treated bars. Before fatigue tests, the specimens were ground by 2000# abrasive paper and well-polished with woolen goods to prevent premature crack initiation at surface machined scratches. The strain-controlled LCF tests were carried out in air on an MTS810 servo-hydraulic fatigue machine at 900 and 1000 °C. A compact two-zone resistance heating furnace (model 653.03A, MTS Systems Corporation, Eden Prairie, MN) with two temperature controllers (MTS 409.83) provides a high temperature environment. During the LCF deformation, the temperature fluctuation over the gauge length was maintained within  $\pm 2^\circ\text{C}$ . Loading was push-pull type triangle with a cyclic frequency of 0.35 Hz. The total strain amplitude varied from 0.5% to 1.2% and R ratio ( $\epsilon_{\min}/\epsilon_{\max}$ ) was -1. At least two specimens were tested at each LCF testing condition and all of them were run to fracture. Finally, the

ruptured specimen is cooling down to room temperature in the air.

In order to observe the deformation mechanisms and fracture modes, the cross and longitudinal sections of the fracture samples were observed by the Zeiss Axio Observer ZIm optical microscope (OM) and INSPECT F50 scanning electron microscope (SEM). The specimens for OM and SEM observation were ground, polished and chemically etched in a solution of 20 ml HCl + 5 g CuSO<sub>4</sub> + 25 ml H<sub>2</sub>O. In addition, the INSPECT F50 SEM was equipped with an Oxford energy dispersive spectrometer (EDS), which was used to qualitatively identify the chemical compositions of precipitated phases in M951G alloy. The average size and volume fraction of  $\gamma'$  phase after deformation under certain fatigue conditions were measured by Image J. The thin foils for transmission electron microscope (TEM) observation were cut normal to the stress axis with a thickness of about 600  $\mu$ m and 5 mm away from the fracture surface, then mechanically ground down to approximately 50  $\mu$ m and electro-polished at 17.5 V in a solution of 10% perchloric acid and 90% ethanol below -20 °C. TEM observations were performed on a JEM 2100 TEM operating at 200KV with a double-tilt specimen holder.

**Table 1**

Nominal composition of M951G alloy (wt%).

W	Mo	Nb	Co	Cr	Al	Hf	others	Ni
6.5	3	2.2	5	9	6	1.5	0.091	Bal

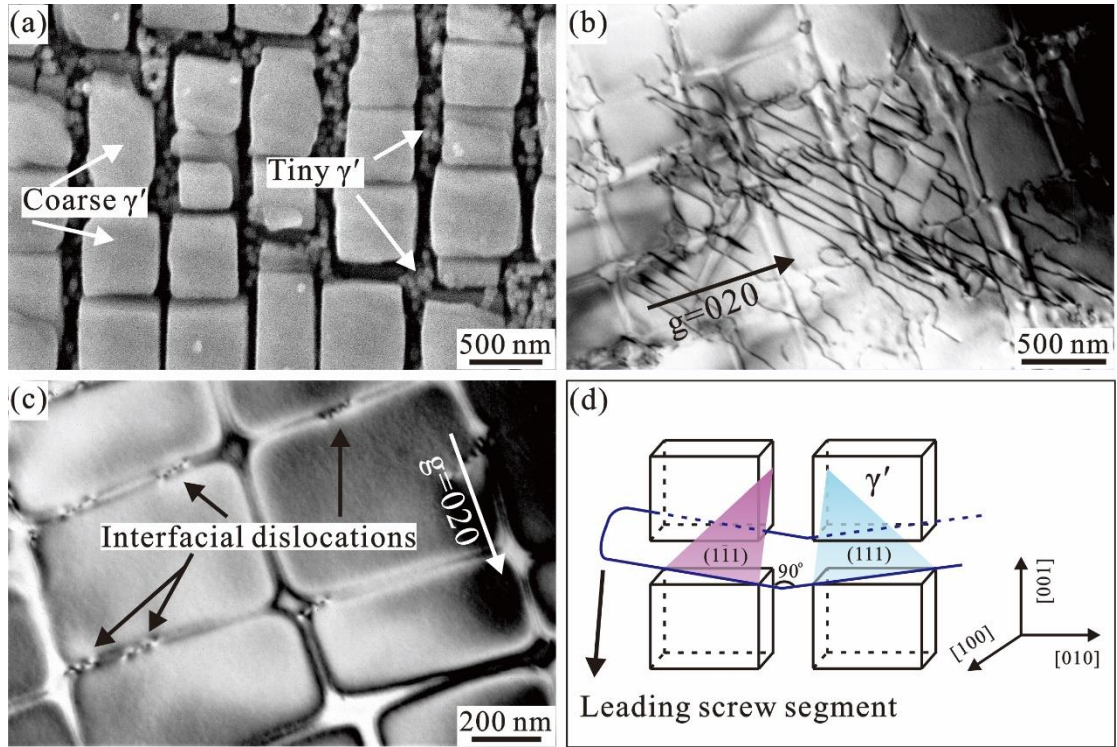


Fig. 1. Typical morphology of  $\gamma'$  precipitates in heat-treated microstructures of M951G alloy.

(a) SEM images; (b) and (c) Two-beam TEM bright-field (BF) images showing dislocation configurations of M951G alloy after heat treatment; (d) Schematic illustration of zig-zag dislocations. All TEM images were taken close to the  $[001]$  zone axis.

### 3. Results

#### 3.1. LCF behavior

Fig. 2 presents various LCF curves of M951G alloy at 900 and 1000 °C. By comparing the cyclic stress response curves of M951G alloy with total strain amplitude ranging from 0.5% to 1.2%, it can be clearly observed that at 900 °C M951G alloy exhibits higher stress amplitude and longer fatigue life than that at 1000 °C. For instance, at  $\Delta\epsilon_t=0.5\%$  the fatigue life at 900 °C is one time longer than that at 1000 °C and the cyclic stress amplitude is about 56 MPa higher. In addition, the relationship between LCF lives and total strain amplitudes of M951G alloy at different testing temperatures are summarized in Fig. 2e. It can be clearly seen that M951G



alloy has longer fatigue life under any strain amplitude at 900 °C, illustrating that testing temperature has a significant impact on the fatigue behavior of the alloy. In the following sections, the effects of testing temperature on the fatigue properties of M951G alloy will be further discussed by taking the microstructural degradations and deformation mechanisms into account.

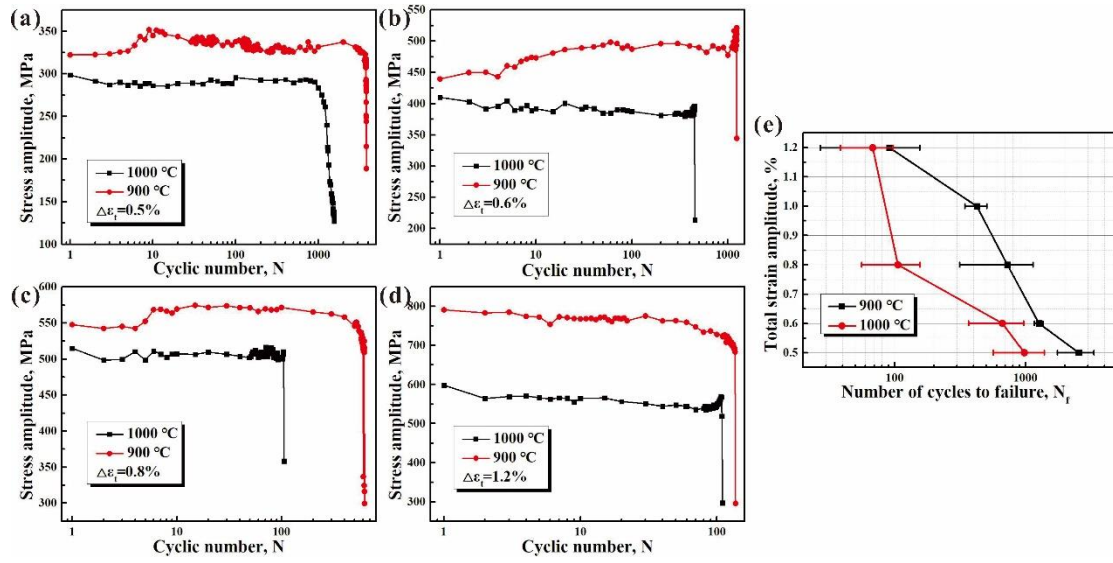


Fig. 2. Cyclic stress response curves of M951G alloys under different total strain amplitudes at 900 and 1000 °C. (a)  $\Delta\epsilon_t=0.5\%$ . (b)  $\Delta\epsilon_t=0.6\%$ . (c)  $\Delta\epsilon_t=0.8\%$ . (d)  $\Delta\epsilon_t=1.2\%$ . (e)  $\Delta\epsilon_t$ - $N_f$  curves of M951G alloy at different testing temperatures.

### 3.2. Fracture Surface Characterization

#### 3.2.1. Microstructures after LCF deformation at 900 °C

The typical fractographies of M951G alloy after LCF tests at 900 °C under different total strain amplitudes are displayed in Fig. 3. As displayed in Fig. 3a and h, LCF fractographies at 900 °C are fractures without obvious plastic deformation and the fracture process can be generally divided into three stages: crack initiation, propagation and final rupture regime. The main feature of the crack initiation stage is the formation of 'facet', which is caused by the crack

initiation at the stress concentration (mainly oxidized carbides, oxides and casting pores) and subsequent propagation along the  $\{111\}$  plane [54, 55], as shown in Fig. 3b. The distinguishable feature of crack propagation stage is relatively flat surfaces and fatigue striations (Fig. 3c and k), which are believed to be produced by the extension of microcrack cycle-by-cycle and can be used to estimate the crack propagation rate by measuring the average spacing between the adjacent striations [56, 57]. However, the final rupture stage features ductile fracture surface (dimples, as shown in Fig. 3f and m), visible dendritic structures (Fig. 3d and l), micropores (Fig. 3g and n) and tire patterns (Fig. 3e). The micropores on the final rupture region are considered to be formed by the coalescence of casting pores via the aggregation of vacancies [7, 58, 59]. Two crack nucleation mechanisms are observed on the fracture surfaces: Majority of cracks form at the oxides (identified as oxidized carbides by EDS in Section 3.2.3) on the specimen surface (Fig. 3b and i) and some cracks nucleate at casting pores at subsurface (Fig. 3j). These mechanisms are consistent with the observations in the literature [23, 29, 43]. Ultimately, the longitudinal sections of the fracture samples are also observed using SEM to study the crack propagation path, as shown in Fig. 3o, p and q. It can be found that the fracture mode varies with strain amplitude increasing. At low strain amplitude ( $\Delta\epsilon_t=0.5\%$ ), the crack propagates intergranularly (Fig. 3o), while the propagation of cracks contain both transgranular (Fig. 3q) and intergranular mode (Fig. 3p) when the total strain amplitude rises to a high level ( $\Delta\epsilon_t=1.2\%$ ). The yellow dashed lines in Fig. 3 are used to separate the crack propagation region from the final rupture region.

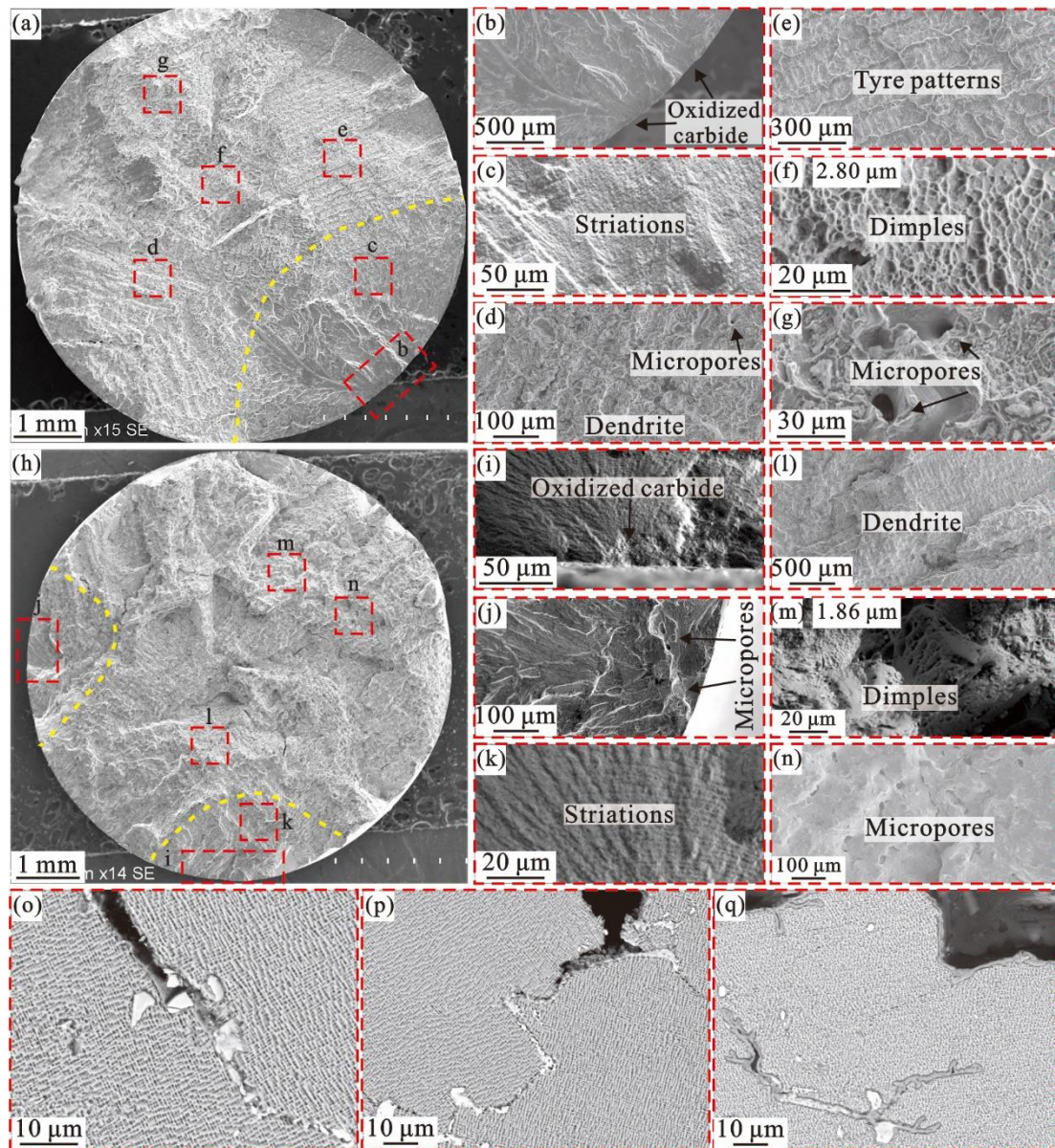


Fig. 3. The typical fractographies of M951G alloy after LCF tests at 900 °C. (a)-(g) Specimens tested under total strain amplitude of 0.5%. (h)-(n) Specimens tested under total strain amplitude of 1.2%. (b)-(g) and (i)-(n) are magnified images in red rectangular areas in (a) and (h), respectively. (o) and (p)-(q) are longitudinal sections of the fracture samples for total strain amplitude of 0.5% and 1.2%, respectively. The black text with white background on the top left corners of Fig. 3(f) and (m) shows the average size of dimples on the fracture surface. (For interpretation of the references to colour in this figure legend, the reader is referred to the Web

version of this article.)

### **3.2.2. Microstructures after LCF deformation at 1000 °C**

The fracture surfaces and the longitudinal sections of the fractures at 1000 °C observed by SEM are exhibited in Fig. 4. Similar to the fractographies observed at 900 °C, the fracture process at 1000 °C also consists of three distinctive stages: crack initiation, propagation and final rupture regime (Fig. 4a and h). Furthermore, fatigue striations (Fig. 4c, d and j), dendrites (Fig. 4e and k) as well as dimples (Fig. 4f and l) also can be observed on the fracture surfaces. It should be emphasized here that some fracture features are different from fatigue fracture at 900 °C: (i) The fracture surfaces are relatively rough (Fig. 4a and h), and the size of dimples is larger (Fig. 4f and l). Besides, higher degrees of plastic deformations occurred after specimens fatigue tests at 1000 °C (Fig. 4a and h) (ii) With the temperature increasing from 900 to 1000 °C, significant oxide layer formed on the fracture surfaces (Fig. 4c and j), illustrating that the effect of oxidation damage on the crack propagation becomes more significant at 1000 °C. Fig. 4g, m and n show the longitudinal sections of the fracture samples, which are used to observe the fracture mechanisms of M951G alloy under different fatigue conditions. Similar to the fracture characteristic observed at 900 °C, it shows a transition from intergranular cracking (Fig. 4g) to a mixed mode of transgranular (Fig. 4n) and intergranular (Fig. 4m) as the total strain amplitude increases from 0.5% to 1.2%.



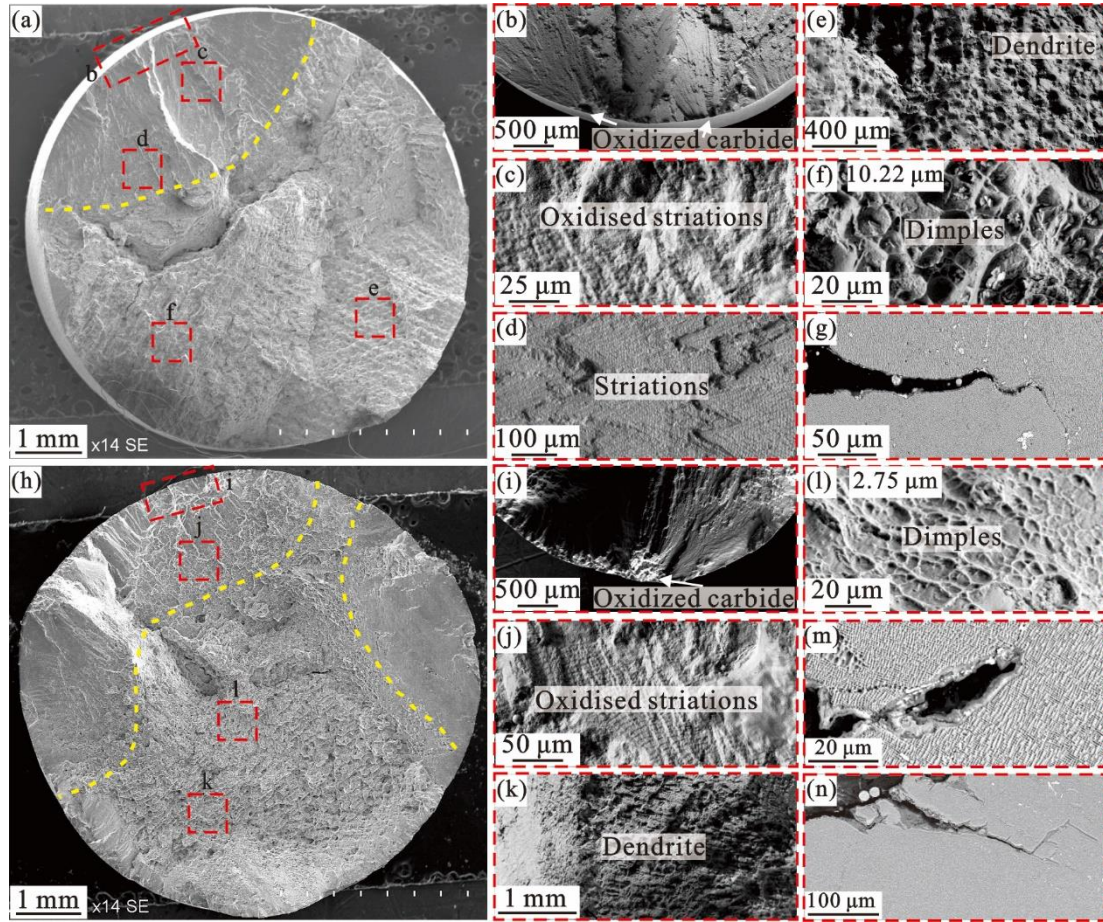


Fig. 4. The typical fractographies of M951G alloy after LCF tests at 1000 °C. (a)-(g) Specimens tested under total strain amplitude of 0.5%. (h)-(n) Specimens tested under total strain amplitude of 1.2%. (b)-(f) and (i)-(l) are magnified images in red rectangular areas in (a) and (h), respectively. (g) and (m)-(n) are longitudinal sections of the fracture samples for total strain amplitude of 0.5% and 1.2%, respectively. The black text with white background on the top left corners of Fig. 4(f) and (l) shows the average size of dimples on the fracture surface. (For interpretation of the references to colour in this figure legend, the reader is referred to the Web version of this article.)

### 3.2.3. Surface oxidation and crack initiation source

Uniform and dense oxide layers were formed on the sample surface after LCF

deformations at high temperature, as shown in the representative images in Fig. 5a-c. No  $\gamma'$  precipitates exist in the surface oxide layer, namely, a precipitation free zone (PFZ) is formed on the sample surface. Moreover, nearly no broken oxide layer was observed and the oxides in the layer did not induce the formation of microcracks. Apart from morphology, the chemical compositions of the oxide layers were also studied by SEM equipped with energy dispersive spectrometer (EDS), and the results were present in Fig. 6. Our compositional mapping reveals that a layer of  $\text{Al}_2\text{O}_3$  was formed on the sample surface. Therefore, M951G alloy has excellent resistance to high temperature oxidation during LCF deformations and the oxide layer formed on the sample surface does not act as the nucleation site for cracks.

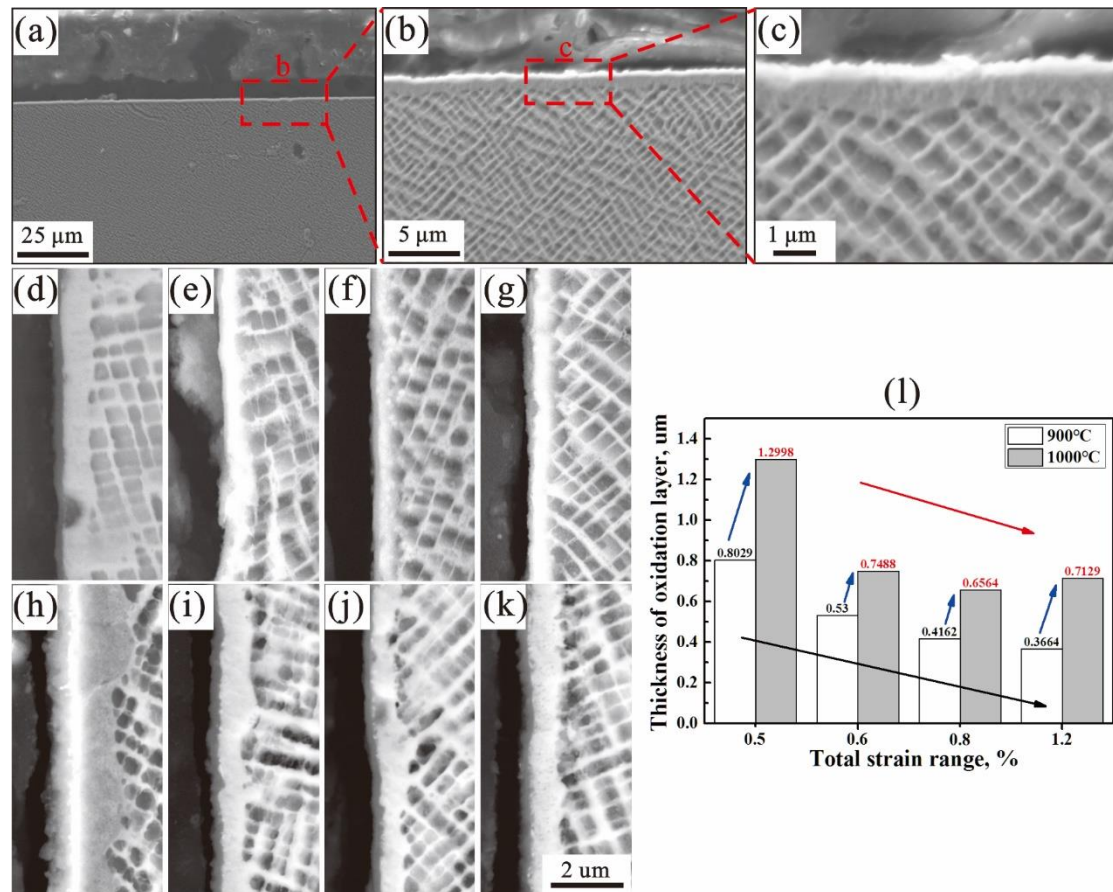


Fig. 5. SEM micrographs showing the oxidation layers at surfaces of M951G alloy after fatigue tests under different conditions. (a)-(c) Representative SEM images of oxidation layers for



M951G alloy after fatigue test (900 °C/ $\Delta\epsilon_t=0.5\%$ ). (d)-(g) Samples fatigue tests at 900 °C under total strain amplitude of 0.5%, 0.6%, 0.8% and 1.2%, respectively. (h)-(k) Samples fatigue tests at 1000 °C under total strain amplitude of 0.5%, 0.6%, 0.8% and 1.2%, respectively. (l) The relationship between thickness of oxidation layer and total strain amplitude of M951G alloy at 900 and 1000 °C.

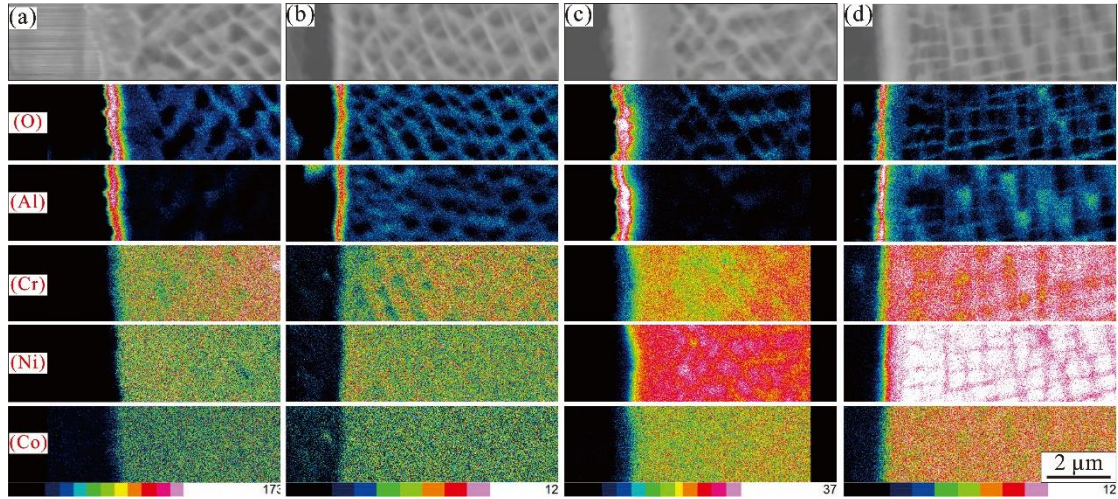


Fig. 6. Energy-dispersive X-ray spectroscopy (EDS) mapping of oxidation layers for M951G alloy after fatigue tests under different conditions, including SEM image, O element, Al element, Cr element, Ni element and Co element. (a) 900 °C/ $\Delta\epsilon_t=0.5\%$ . (b) 900 °C/ $\Delta\epsilon_t=1.2\%$ . (c) 1000 °C/ $\Delta\epsilon_t=0.5\%$ . (d) 1000 °C/ $\Delta\epsilon_t=1.2\%$ . The curved oxide layer in the EDS image is caused by the drift of the sample during the examination.

Fig. 5d-k illustrate the surface oxidation layers of M951G alloy in the metallographic sectioned specimens after fatigue tests under different conditions. At the same testing temperature, the thickness of oxidation layer decreases with the increase of strain amplitude. For example, at  $\Delta\epsilon_t=0.5\%$  at 900 °C thick oxide layer of about 0.8 μm is formed in M951G alloy; while in the case of  $\Delta\epsilon_t=1.2\%$ , relatively thinner oxide layer of about 0.37 μm forms on the surface, as displayed in Fig. 5d, g and l. On the other hand, by comparing the thickness of

oxidation layer at the same strain amplitude, it can be seen that the oxide thickness increases with the rise of temperature. High-temperature oxidation has a detrimental effect on fatigue properties of nickel-based superalloys by affecting the crack initiation and propagation [50, 60-62]. Research shows that oxide layer has high contents of aluminum and titanium, which results in the depletion of  $\gamma'$  phase along the fatigue crack and accelerates the failure of alloys [35].

In order to further study the preferential crack initiation and propagation of M951G alloy under different fatigue tests, the longitudinal sections of the fracture samples were systematically observed by SEM, as shown in Fig. 7. It can be clearly observed that whether at 900 °C or 1000 °C, the cracks usually initiate on the surface oxides (Fig. 7a, b and g) or eutectics (Fig. 7f) along the grain boundaries under low strain amplitude. The compositions of oxides that cause crack initiation (Fig. 7a, b and g) also have been studied by EDS and the result is listed in Table 2. It can be easily inferred that oxidized carbides (MC type, M=Nb, Hf) promote crack initiation. Previous studies [60, 63] also show that surface carbides are easier to oxidize than the  $\gamma$  matrix, which is due to the superior corrosion resistance of Ni-rich matrix with the solution of Cr, Co, W, Mo, etc [60, 63]. Furthermore, compared with brittle carbides or casting micropores, oxidized carbides may be more susceptible to cracks. This is due to the fact that during the carbide oxidation process, volume expansion will occur, causing the increase of GND (geometrically necessary dislocation) density around the tip of oxidized carbide [54], thus promoting the initiation of cracks. Similar observation was found in other alloys during fatigue tests [64, 65]. Therefore, it can be concluded that the surface oxidized carbides induce crack initiation under low total strain amplitude. On the other hand, at relatively higher strain amplitude, apart from the oxidized carbides and eutectic along the grain boundaries (Fig. 7c



and h), casting micropores (Fig. 7d) and residual eutectics (Fig. 7e) in the grain interior also become the crack initiation sources. In addition, some transgranular cracks are basically perpendicular to the loading axis (Fig. 7i and j) and cut through the  $\gamma'$  precipitates (Fig. 7j), which is consistent with the previous studies [66-68].

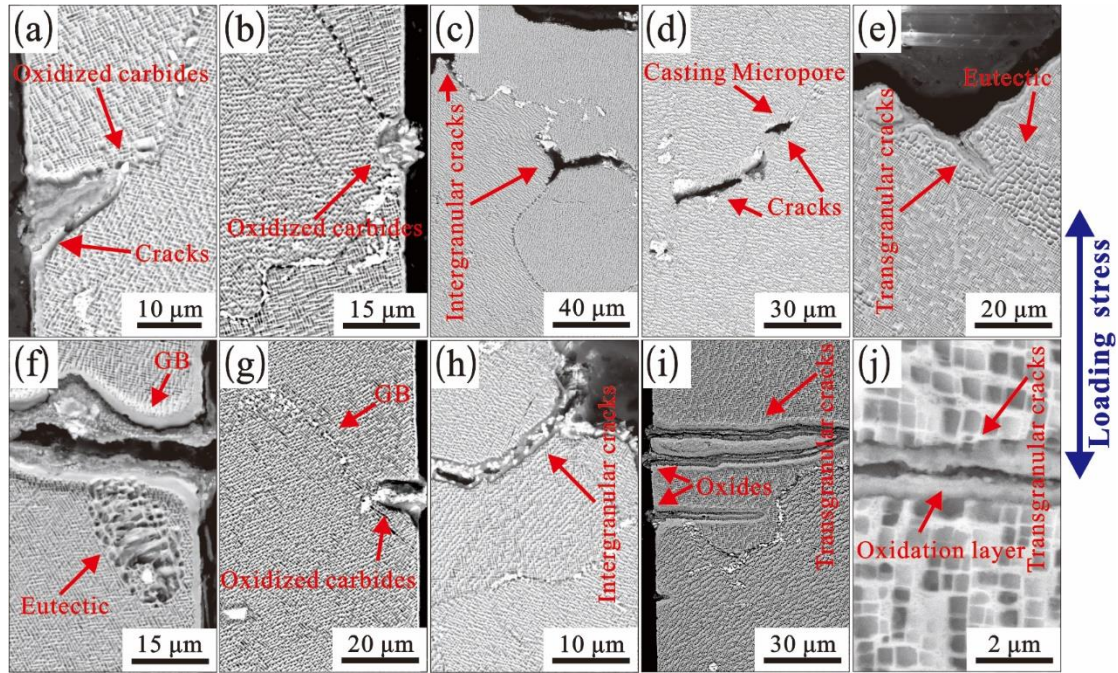


Fig. 7. SEM images showing microcrack initiation sites of M951G alloy under different LCF testing conditions. (a)-(b) 900 °C/ $\Delta\epsilon_f=0.5\%$ . (c)-(e) 900 °C/ $\Delta\epsilon_f=1.2\%$ . (f)-(g) 1000 °C/ $\Delta\epsilon_f=0.5\%$ . (h)-(j) 1000 °C/ $\Delta\epsilon_f=1.2\%$ .

**Table 2.**

The compositions of oxide determined by EDS (wt%).

O	Cr	Co	Nb	Hf	W
23.22	2.86	1.45	24.59	37.84	10.04

### 3.3. Evolutions of $\gamma'$ precipitates

Fig. 8 shows the typical morphologies of  $\gamma'$  precipitates for M951G alloy after LCF tests under different testing conditions. It can be clearly seen that M951G alloy maintains a well

microstructure stability at 900 °C. It means the coarse  $\gamma'$  precipitates basically retain a cubic shape and a great many spherical  $\gamma'$  particles still exist in the narrow matrix channels, as shown in Fig. 8a-d. However, after fatigue testing at 1000 °C, some corners of cubic  $\gamma'$  precipitates appear to be degenerated, and the spherical  $\gamma'$  particles are totally dissolved. Furthermore, by comparing Fig. 8a and d or Fig. 8e and h, the coarsening trend becomes more obvious with the decrease of strain amplitude. Apart from that, the sizes and volume fractions of the cubic  $\gamma'$  phase after different fatigue tests are also calculated and plotted in Fig. 9a and b, which are the result of statistical calculations from at least 20 different representative areas for each sample deformed at specific fatigue conditions. In present study, the area fraction of cubic  $\gamma'$  phase is treated as the volume fraction and  $\gamma'$  precipitates are considered to be cubes. Average edge length of  $\gamma'$  precipitates ( $D_1$ ) is calculated as follows:

$$D_1 = \sqrt{\frac{S_1}{n_1}} \quad (1)$$

Where  $S_1$  and  $n_1$  are the total area and number of  $\gamma'$  precipitates in the selected image. At the same testing temperature with the strain amplitude decreasing, or at the same strain amplitude as the testing temperature rises, the average edge length of cubic  $\gamma'$  precipitates increases (Fig. 8a), while the volume fraction of cubic  $\gamma'$  phase is decreased (Fig. 8b). In a word, testing temperature and strain amplitude have a significant effect on the evolution of  $\gamma'$  precipitates, and the size of the  $\gamma'$  phase is an important parameter for fatigue properties of the superalloys. Therefore, the changes of cubic  $\gamma'$  precipitates will be analyzed from the aspects of testing temperature and total strain amplitude in Section 4.3.

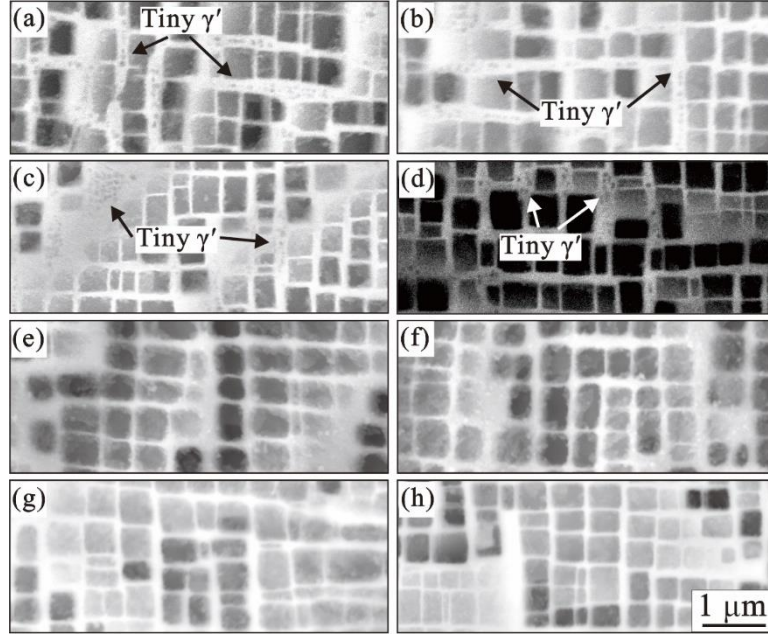


Fig. 8. Morphologies of  $\gamma'$  precipitates for M951G alloy after LCF tests at different testing conditions. (a)-(d) Samples fatigue tests at 900 °C under total strain amplitude of 0.5%, 0.6%, 0.8% and 1.2%, respectively. (e)-(h) Samples fatigue tests at 1000 °C under total strain amplitude of 0.5%, 0.6%, 0.8% and 1.2%, respectively.

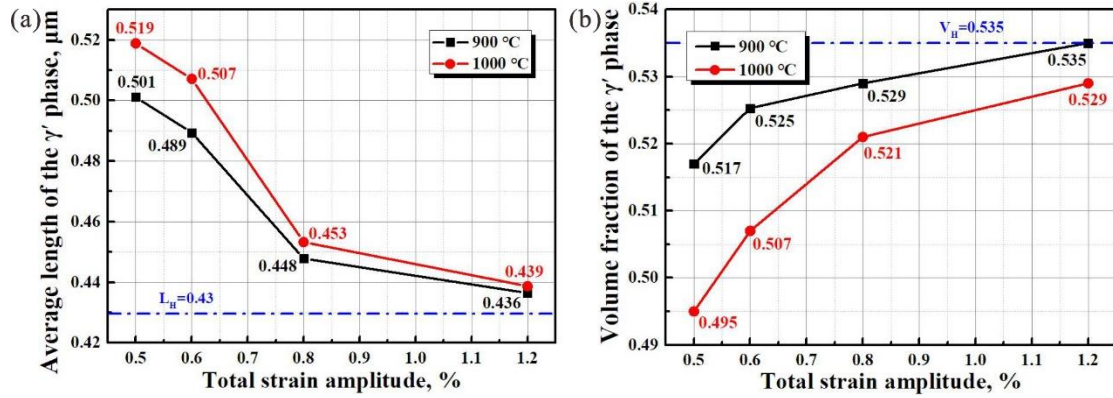


Fig. 9. (a), (b) Statistical sizes and volume fraction of the cubic  $\gamma'$  phase after LCF tests under different testing conditions.  $L_H$  in Fig. 9a and  $V_H$  in Fig. 9b represent the average edge length and statistical volume fraction of the cubic  $\gamma'$  phase after heat treatment, respectively.

## 4. Discussion

### 4.1. The effects of testing temperature on fatigue properties of M951G alloy

In present work, as displayed in Fig. 2, fatigue life and cyclic stress response of M951G alloy under the same total strain amplitude at 900 °C are significantly higher than that at 1000 °C, which illustrates the fatigue property has a high dependency on the testing temperature. As it is commonly known, both the interaction between dislocations and the interaction between dislocations and precipitates constitute the resistance of nickel-based superalloys to plastic deformation in the low cycle fatigue test [69-72]. The following will explain the fatigue performance differences of M951G alloy at 900 and 1000 °C in terms of deformation microstructures and dislocation configurations.

Fig. 10 shows the microstructures and corresponding schematic illustration of deformation mechanisms for M951G alloy after fatigue tests at 900 °C under different total strain amplitudes. It can be clearly observed that the  $\gamma'$  precipitates maintain a well cubic shape and the width of  $\gamma$  channels remains relatively narrow after fatigue tests at 900 °C. In addition, similar to the heat treatment microstructure (Fig. 1a), a large number of spherical  $\gamma'$  particles still exist in  $\gamma$  matrix channels, as illustrated in Fig. 10c and e. However, as the testing temperature increases to 1000 °C, the cuboidal  $\gamma'$  precipitates have a tendency to coarsen and the spherical  $\gamma'$  particles are inclined to disappear (Fig. 11), therefore the  $\gamma$  channel width is significantly increased and partial coherent  $\gamma/\gamma'$  interfacial stress has been released. The microstructure degradation of M951G alloy at 1000 °C weakens the order precipitation contribution to strengthening of alloy, which significantly reduces the cyclic stress and accelerates the fatigue fracture. On the other hand, the densities of shearing dislocations in  $\gamma'$  precipitates under different fatigue conditions are also calculated and presented in Fig. 13. The shearing dislocation density is the result of statistical calculations from at least 50 different representative areas for each sample deformed

at specific fatigue conditions. As displayed in Fig. 13, the density of shearing dislocations (including  $a/3 \langle 112 \rangle$  partial dislocations and APBs) in  $\gamma'$  phase obviously increases with the increase of testing temperature at the same strain amplitude. It may be due to the degradation of microstructures and partial loss of coherency of  $\gamma/\gamma'$  interfaces. The repeated shearing of  $\gamma'$  precipitates by dislocations through the ordered lattice during fatigue tests also reduces the fatigue life and cyclic stress response of M951G alloy. Apart from the microstructural degradations and deformation mechanisms, the formation of brittle oxides also plays a key role on the fatigue properties of M951G alloy [29, 73, 74]. As illustrated in Fig. 4c and j or Fig. 5, under the same total strain amplitude with the testing temperature increasing from 900 °C to 1000 °C, the thickness of oxidation layer evidently increases, which may induce a weak stress response [73, 74] and decrease the fatigue life [29]. Furthermore, the plastic strain at 1000 °C is obviously higher than that of 900 °C at the same total strain amplitude, as demonstrated in Fig. 12. The plastic strain amplitude ( $\Delta \varepsilon_p/2$ ) in a certain cyclic deformation is calculated to be the average value of intercepts ( $\Delta \varepsilon_A$  and  $\Delta \varepsilon_B$ ) at the strain axis, as shown in Fig. 14(a) and (b). The larger the plastic deformation is, the more secondary crack initiation appears and the shorter the fatigue life is [44]. This is consistent with the higher density of shearing dislocations in the  $\gamma'$  precipitates at 1000 °C under the same strain amplitude as mentioned above. According to the above discussion, it can be concluded that the degradation of microstructures, greater number of shearing dislocations in the  $\gamma'$  phase and higher degree of oxidation are the main reasons for the decrease of fatigue life as well as cyclic stress response with the testing temperature increasing.



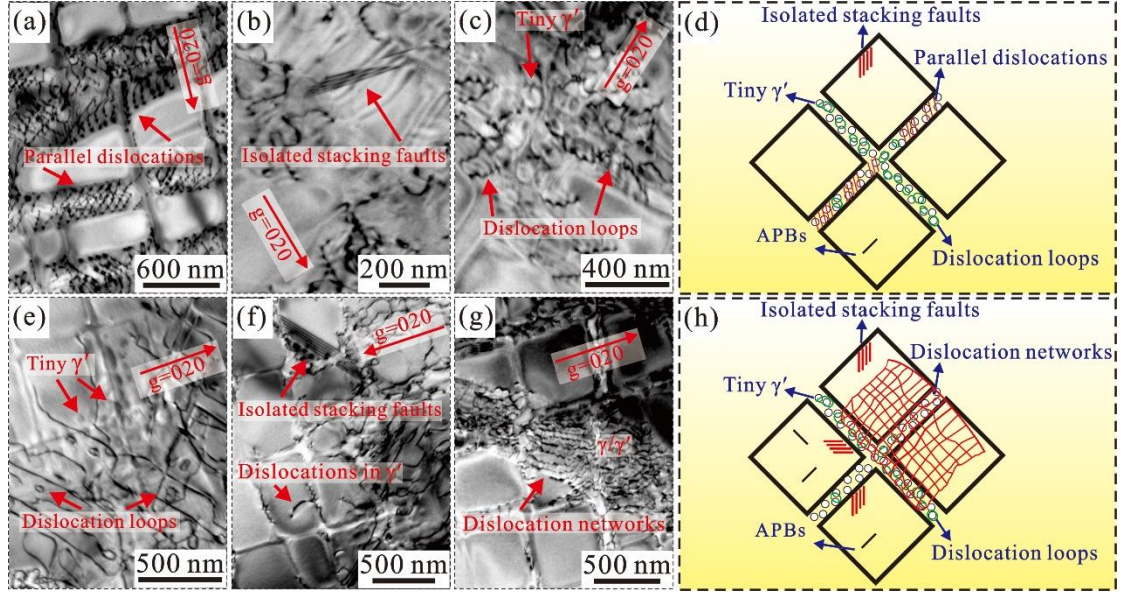


Fig. 10. Deformation microstructures and dislocation configurations of M951G alloy after fatigue tests at 900 °C. (a)-(c)  $\Delta\epsilon_t=0.5\%$ . (e)-(g)  $\Delta\epsilon_t=1.2\%$ . (d) and (h) are schematic illustrations of the deformation mechanism for M951G alloy at 900 °C under total strain amplitude of 0.5% and 1.2%, respectively. All images were taken close to the  $[001]$  zone axis.

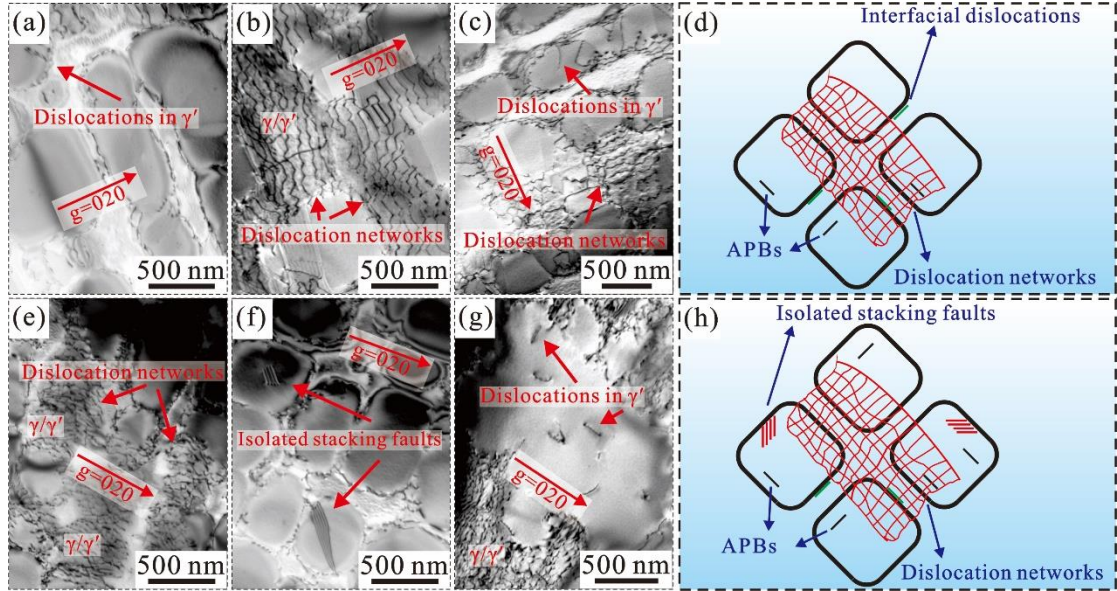


Fig. 11. Deformation microstructures and dislocation configurations of M951G alloy after fatigue tests at 1000 °C. (a)-(c)  $\Delta\epsilon_t=0.5\%$ . (e)-(g)  $\Delta\epsilon_t=1.2\%$ . (d) and (h) are schematic illustrations of the deformation mechanism for M951G alloy at 1000 °C under total strain

amplitude of 0.5% and 1.2%, respectively. All images were taken close to the [001] zone axis.

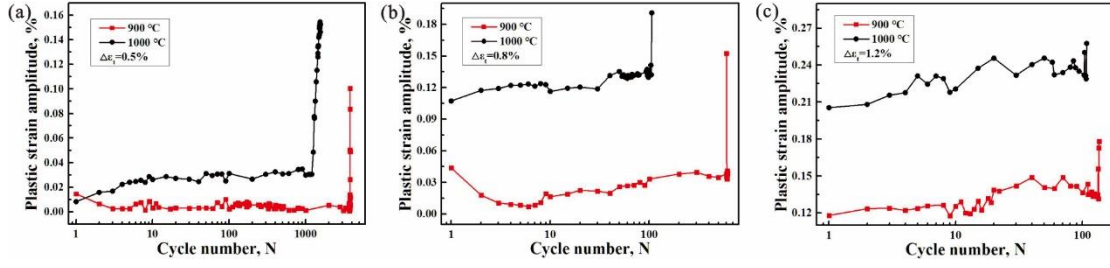


Fig. 12. The relationship between plastic strain amplitude and cyclic number for M951G alloy under different testing conditions.

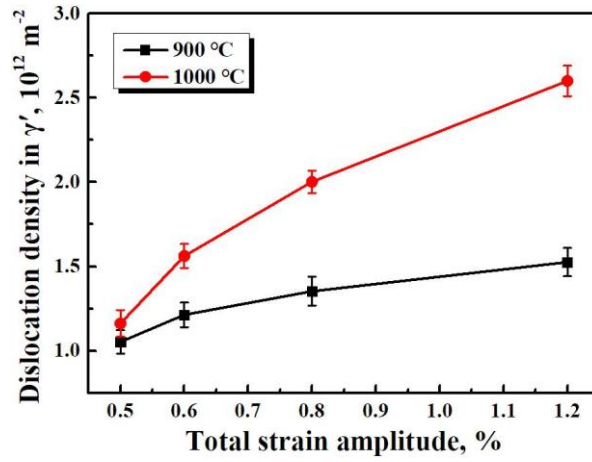


Fig. 13. Density of shearing dislocations (including isolated stacking faults and APBs) in  $\gamma'$  precipitates vs. deformation temperature. The error bars correspond to the standard deviation.

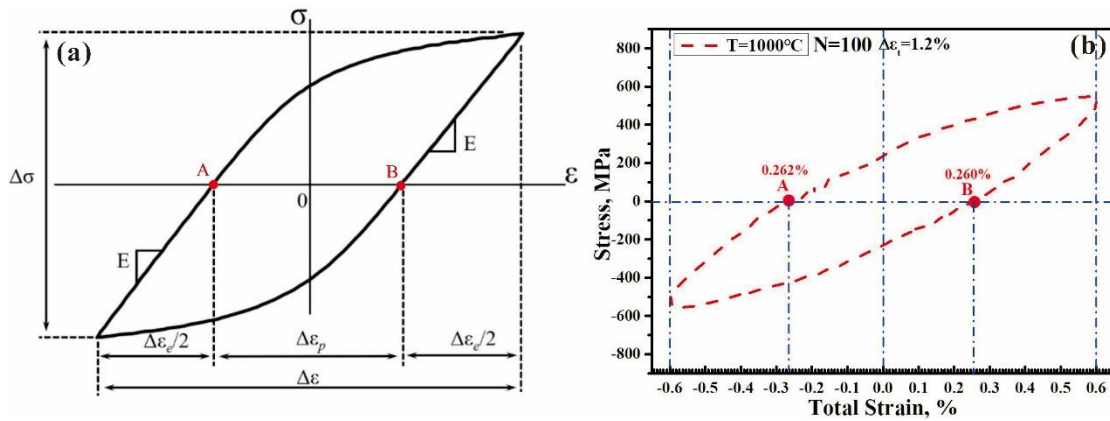


Fig. 14. (a) Schematic illustration of hysteresis loop for M951G alloy during LCF deformation.

(b) Hysteresis loop of the 100th LCF deformation for M951G alloy under 1000 °C total strain

amplitude of 1.2%; the plastic strain amplitude is calculated to be 0.261%.

## **4.2. The fatigue fracture modes**

Significantly different fracture mechanisms have been observed after failure under various fatigue conditions, as presented in Fig. 3 and Fig. 4. Whether the temperature is at 900 or 1000 °C, the fracture mechanism is intergranular cracking (Fig. 3o and 4g) at relatively low strain amplitude; while it changes to a mixed mode of transgranular and intergranular as the strain amplitude increases to a high level (Fig. 3p, q and 4m, n).

At low strain amplitude, as the fatigue samples are exposed in high temperature for a long time, the surfaces of the alloy are severely oxidized (Fig. 5d and h) and the cracks mainly initiate at the oxidized carbides and eutectics near the grain boundaries on the sample surfaces, as shown in Fig. 7a, b, f and g. Compared with brittle carbides and casting micropores, oxidized carbides are more likely to induce crack initiation due to the volume expansion during oxidation and the increase of stress concentration around oxidized carbides [54]. On the other hand, as it is commonly known that the casting micropores are mainly distributed at the final solidification stage of the alloy, such as grain boundaries and interdendritic regions. In the present study, the statistical grain size of M951G alloy is about 3.273 mm (the standard deviation is 1.435 mm), which means the grain boundary content is very low [7]. Therefore, most of casting micropores are located in the interdendritic regions, only a small amount along the grain boundaries. Hence, nearly no micropores along the grain boundaries act the nucleate site. Moreover, deformation rate also plays a key role in determining fracture behavior of M951G alloy during fatigue tests. As reported in Ref. [75, 76], when the deformation rate is relatively low, the alloy mainly undergoes intergranular fracture. In present study, the low strain amplitude corresponds to a



low strain rate since the loading stress cyclic frequency is a constant (0.35 Hz). Therefore, fatigue cracks are more inclined to initiate from the oxidized carbides and then propagate along the grain boundaries, finally resulting in a typical intergranular cracking at low strain amplitude. However, as the strain amplitude increases to a high level, not only the surface oxidized carbides (Fig. 7c and h) are the source of cracks, but also the casting micropores (Fig. 7d) in the grain interior, the interdendritic broken carbides and residual eutectics (Fig. 7e) become the crack initiation sources. Additionally, for the experimental alloy in present work, majority of eutectics and carbides are distributed in interdendritic regions, and the mean size of interdendritic carbides is much larger than that along the grain boundaries [7]. Therefore, microcracks have more probabilities to initiate within the grain interior, and finally promote the formation of transgranular cracks. On the other hand, as shown in Fig. 13, the density of isolated stacking faults and APBs in  $\gamma'$  precipitates increases with the increase of strain amplitude at the same testing temperature, which can result in inhomogeneous deformation in local regions [29] and also has a certain effect on the promotion of transgranular cracking. Apart from that, other conditions such as strain amplitude and cyclic strain rate also should be fully considered. As described above, the loading stress cyclic frequency is a constant in present work and the higher strain amplitude corresponds to a higher strain rate. The research conducted by Dong [76] shows that there is a transition of fracture mechanisms from intergranular cracking to intragranular cracking with the strain rate increasing. The grain boundary sliding is the main way for the low solvus, high refractory (LSHR) superalloy to plastically deform under relatively lower strain rate [76]. However, as the strain rate is rapid enough, grain boundary sliding cannot keep up with the deformation in the grain interior. Strain concentration is prone to form in local

regions of grain, which promotes the occurrence of intragranular fracture [76]. Similar phenomenon also has been reported by Guan in a newly developed Ni-Fe-Cr-based superalloy [75]. Consequently, the distribution of broken carbides and eutectics, inhomogeneous deformation in local regions and relatively higher strain rate are the main reasons for the formation of transgranular microcracks under large strain amplitude.

### 4.3. The effects of testing conditions on the coarsening of cubic precipitates

As reported in Ref. [67, 77], the coarsening process of  $\gamma'$  precipitates is related to the time exposed to high temperature and the amount of strain accumulation. In present study, the relationship between the average size of cubic  $\gamma'$  precipitates and exposure time in high temperature is in accordance with the Lifshitz–Slyozov–Wagner (LSW) model [78, 79], as plotted in Fig. 15a. Therefore, the coarsening kinetics of cubic  $\gamma'$  precipitates during fatigue deformation can be described as follows:

$$d^3 - d_0^3 = kt \quad (1)$$

$$k = (8\gamma DC_e V_m) / (9RT) \quad (2)$$

where  $d$  is the mean size of cubic  $\gamma'$  precipitates at time  $t$ ;  $d_0$  is the mean size of cubic  $\gamma'$  precipitates after heat treatment;  $k$  is the rate constant;  $\gamma$  is the interfacial energy between precipitate and matrix;  $D$  is the diffusion coefficient of the solute in the matrix;  $C_e$  is the equilibrium concentration of solute in the matrix;  $V_m$  is the molar volume of  $\gamma'$  phase;  $R$  is the universal gas constant and  $T$  is the absolute temperature.

As presented in Fig. 8, the microstructure of superalloy consists of a disordered solid solution  $\gamma$  matrix with fcc structure and a high volume fraction of the ordered  $\gamma'$  precipitates with  $L1_2$  structure. Thus, M951G alloy can be considered as a composite composed of hard  $\gamma'$

phase and soft matrix phase [80, 81] and the total external stress ( $\sigma_e$ ) is shared by the two phases, so the total external stress can be expressed as follows:

$$\sigma_e = (1-\varphi)\sigma_\gamma + \varphi\sigma_{\gamma'} \quad (3)$$

where  $\varphi$  is the volume fraction of  $\gamma'$  phase;  $\sigma_\gamma$  and  $\sigma_{\gamma'}$  represent the local flow stress of  $\gamma$  and  $\gamma'$  phases, respectively. In addition, it also has been reported that the flow stress difference ( $\Delta\sigma_D$ ) between the two phases promotes the diffusion of elements and induces the growth of  $\gamma'$  precipitates [48, 82], and the size of  $\gamma'$  precipitates as a function of flow stress difference is as below:

$$\Delta\sigma_D = \sigma_{\gamma'} - \sigma_\gamma = m d \quad (4)$$

where  $m$  is a parameter related to the lattice misfit between  $\gamma$  and  $\gamma'$  phases. When the alloy is unloaded ( $\sigma=0$ ,  $d=d_0$ ), according to Eqs. (3) and (4), we can get

$$\sigma_\gamma = -m\varphi d_0 \quad (5)$$

Moreover, based on the Eqs. (3), (4) and (5), the relationship between size of  $\gamma'$  precipitates and total external stress can be expressed as follows:

$$d - d_0 = \frac{\sigma_e}{m\varphi} \quad (6)$$

Furthermore, according to the Eqs. (1) and (6), we can get the equation as follows:

$$d^2 + d_0 d + d_0^2 = km\varphi t / \sigma_e \quad (7)$$

On the other hand, in present work, the loading stress cyclic frequency ( $f$ ) is a constant (0.35 Hz), thus the whole exposure time in high temperature can be described as follows:

$$t = \frac{N_f}{f} \quad (8)$$

Then, substituting Eq. (8) into Eq. (7), we can get equation as below:

$$d = \sqrt{\frac{km\varphi N_f}{f\sigma_e} - \frac{3}{4}d_0^2} + \frac{d_0}{2} \quad (9)$$

In addition,  $K=km/f\sigma_e$  can be called as the growth factor of the cubic  $\gamma'$  phase, which is used to describe the influence of fatigue conditions (testing temperature and strain amplitude) on the size of cubic  $\gamma'$  precipitates. Therefore, Eq. (9) can be simplified as follows:

$$d = \sqrt{K\varphi N_f - \frac{3}{4}d_0^2 - \frac{d_0}{2}} \quad (10)$$

Ultimately, the growth factors of the cubic  $\gamma'$  phase after different fatigue tests are calculated and plotted in Fig. 15b. The results show that both increasing testing temperature and total strain amplitude are conducive for the growth of cubic  $\gamma'$  precipitates during fatigue deformations. From Eq. (10), it is easy to infer that fatigue testing conditions, volume fraction of  $\gamma'$  phase and fatigue life are the main reasons for the variation of  $\gamma'$  phase size. In the present work, the volume fraction of  $\gamma'$  phase and fatigue life are determined by the fatigue testing conditions (Fig. 9). Besides, the size of the  $\gamma'$  precipitates is also an important factor affecting the fatigue performances of superalloys [83]. Therefore, it is necessary to analyze the variation of  $\gamma'$  sizes during fatigue deformations from the aspects of testing temperature and strain amplitude in the following sections.

As displayed in Fig. 9a, the average size of cubic  $\gamma'$  precipitate at 1000 °C is larger than that at 900 °C at the same strain amplitude, which can be rationalized as follows. Higher temperature corresponds to stronger thermal activation and faster element diffusion rate, which results in a larger growth factor of the  $\gamma'$  phase (as present in Fig. 15b) and finally promotes the growth of cubic  $\gamma'$  precipitates. Moreover, the volume fraction of cubic  $\gamma'$  phase significantly decreases with the testing temperature increasing, as illustrated in Fig. 9b. According to the Eqs. (3) and (4), the change in the volume fractions of the  $\gamma$  and  $\gamma'$  phase will cause the variation of local flow stress distribution between them, and finally affects the size of  $\gamma'$  precipitates. Here

it should be noted that, as plotted in Fig. 2e, obviously short fatigue life at 1000 °C restrains the growth of  $\gamma'$  precipitates, but it could not be regarded as a dominating factor when considering the actual size of precipitates, as demonstrated in Fig. 9a. Ultimately, it can be concluded that the variation of local flow stress distribution between the  $\gamma/\gamma'$  interfaces and the higher degree of thermal activation are the major reasons for the large size of cubic  $\gamma'$  precipitates at 1000 °C.

Apart from the testing temperature, other conditions such as strain amplitude also should be fully considered. As shown in Fig. 9a, the average length of cubic  $\gamma'$  precipitates increases with the decrease of strain amplitude, which can be rationalized as follows. At the same testing temperature, lower strain amplitude corresponds to longer high temperature exposure time (Fig. 2d), which is conducive to the growth of precipitates. On the other hand, the great change of flow stress difference between the  $\gamma/\gamma'$  interfaces induced by the high variation of  $\gamma'$  phase volume fraction at low strain amplitude also has certain effects on the  $\gamma'$  phase size. Certainly, the relatively small loading stress under low strain amplitude is a restraining factor for the growth of cubic  $\gamma'$  precipitates. However, the inhibitory effect caused by small loading stress hardly completely compensates the positive impact induced by the longer high temperature exposure time and greater variation of  $\gamma/\gamma'$  interfacial flow stress difference. Therefore, at the same testing temperature, the average size of cubic  $\gamma'$  precipitates increases with the decrease of strain amplitude.

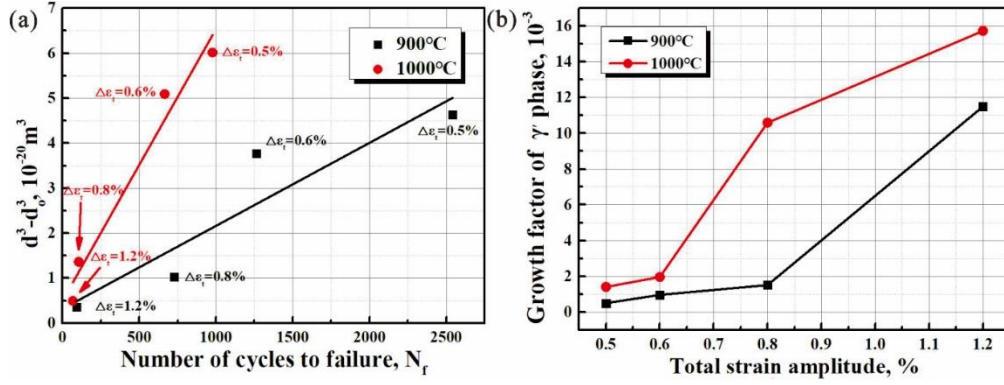


Fig. 15. (a) Plot of precipitate sizes ( $d^3 - d_0^3$ ) vs. number of cycles to failure. (b) The growth factor of the cubic  $\gamma'$  phase for M951G alloy under different strain amplitudes at 900 and 1000 °C.

## 5. Conclusions

The LCF properties of M951G alloy under different total strain amplitudes at 900 and 1000 °C have been systematically studied using OM, SEM and TEM. The differences of fatigue life, cyclic stress response and fracture characteristics as well as coarsening of  $\gamma'$  precipitates under different fatigue conditions have been analyzed in detail. The main conclusions obtained in present work are listed as follows:

- (1) The fatigue life and cyclic stress response of M951G alloy under the same total strain amplitude at 1000 °C are significantly lower than that at 900 °C, which is due to the degradation of microstructures, greater number of shearing dislocations in the  $\gamma'$  precipitates and higher degree of oxidation.
- (2) At low strain amplitude, the fracture mode is intergranular cracking, which is due to the increase of stress concentration around oxidized carbides during the oxidation process and the relatively low deformation rate. At high strain amplitude, the fracture mode turns to a mixed type of transgranular and intergranular. The distribution of broken carbides and

eutectics, inhomogeneous deformation in local regions and relatively high strain rate are the main reasons for the formation of transgranular microcracks.

- (3) At the same strain amplitude, the average size of cubic  $\gamma'$  precipitates at 1000 °C is larger than that at 900 °C. The variation of flow stress differences between the  $\gamma/\gamma'$  interfaces and the higher degree of thermal activation are supposed to be responsible for it.
- (4) At the same testing temperature, the average size of cubic  $\gamma'$  precipitates increases with the decrease of strain amplitude, which is due to the long exposure time in high temperature and great variation of  $\gamma/\gamma'$  interfacial flow stress difference at low strain amplitude.

## Acknowledgments

This work was financially supported by the National Natural Science Foundation of China (NSFC) under Nos. 51971214 and 51771191. The authors are grateful for those supports.

## References

- [1] J.X. Zhang, T. Murakumo, H. Harada, Y. Koizumi, Dependence of creep strength on the interfacial dislocations in a fourth generation SC superalloy TMS-138, *Scr. Mater.* 48(3) (2003) 287-293.
- [2] J.X. Zhang, T. Murakumo, Y. Koizumi, T. Kobayashi, H. Harada, Slip geometry of dislocations related to cutting of the  $\gamma'$  phase in a new generation single-crystal superalloy, *Acta Mater.* 51(17) (2003) 5073-5081.
- [3] J.S. Van Sluytman, T.M. Pollock, Optimal precipitate shapes in nickel-base  $\gamma$ - $\gamma'$  alloys, *Acta Mater.* 60(4) (2012) 1771-1783.
- [4] X.G. Wang, J.L. Liu, T. Jin, X.F. Sun, Y.Z. Zhou, Z.Q. Hu, J.H. Do, B.G. Choi, I.S. Kim, C.Y. Jo, Deformation mechanisms of a nickel-based single-crystal superalloy during low-cycle fatigue at different temperatures, *Scr. Mater.* 99 (2015) 57-60.
- [5] M. Yang, J. Zhang, H. Wei, W. Gui, H. Su, T. Jin, L. Liu, A phase-field model for creep behavior in nickel-base single-crystal superalloy: Coupled with creep damage, *Scr. Mater.* 147 (2018) 16-20.
- [6] L. Cui, J. Yu, J. Liu, X. Sun, Cyclic stress responses of a newly developed nickel-base superalloy at elevated temperatures, *J. Alloys Compd.* 773 (2019) 250-263.
- [7] L. Cui, J. Yu, J. Liu, X. Sun, Microstructural evolutions and fracture behaviors of a newly developed nickel-base superalloy during creep deformation, *J. Alloys Compd.* 746 (2018) 335-349.
- [8] X. Zhang, T. Jin, N.R. Zhao, Z.H. Wang, X.F. Sun, H.R. Guan, Z.Q. Hu, Effect of strain rate on the tensile behavior of a single crystal nickel-base superalloy, *Mater. Sci. Eng. A* 492(1-2) (2008) 364-369.
- [9] P. Li, B.M. Zhou, Y.Z. Zhou, J.G. Li, T. Jin, X.F. Sun, Z.F. Zhang, Effect of orientations on in situ tensile deformation and fracture behaviours of nickel-base single-crystal superalloys, *Philos. Mag.* 94(21)

(2014) 2426-2446.

- [10] L. Shi, J.J. Yu, C.Y. Cui, X.F. Sun, Microstructural stability and tensile properties of a Ti-containing single-crystal Co-Ni-Al-W-base alloy, *Mater. Sci. Eng. A* 646 (2015) 45-51.
- [11] X. Xiong, P. Dai, D. Quan, Z. Wang, Q. Zhang, Z. Yue, Intermediate temperature brittleness and directional coarsening behavior of nickel-based single-crystal superalloy DD6, *Mater. Des.* 86 (2015) 482-486.
- [12] F. Sun, Y.F. Gu, J.B. Yan, Z.H. Zhong, M. Yuyama, Tensile deformation-induced dislocation configurations at intermediate temperatures in a Ni-Fe-based superalloy for advanced ultra-supercritical coal-fired power plants, *J. Alloys Compd.* 657 (2016) 565-569.
- [13] J. Liu, W. Tang, J. Li, Deformation and fracture behaviors of K403 Ni-based superalloy at elevated temperatures, *J. Alloys Compd.* 699 (2017) 581-590.
- [14] P. Zhang, Y. Yuan, S.C. Shen, B. Li, R.H. Zhu, G.X. Yang, X.L. Song, Tensile deformation mechanisms at various temperatures in a new directionally solidified Ni-base superalloy, *J. Alloys Compd.* 694 (2017) 502-509.
- [15] F. Sun, Y.F. Gu, J.B. Yan, Z.H. Zhong, M. Yuyama, Phenomenological and microstructural analysis of intermediate temperatures creep in a Ni-Fe-based alloy for advanced ultra-supercritical fossil power plants, *Acta Mater.* 102 (2016) 70-78.
- [16] H. Long, Y. Liu, D. Kong, H. Wei, Y. Chen, S. Mao, Shearing mechanisms of stacking fault and anti-phase-boundary forming dislocation pairs in the  $\gamma'$  phase in Ni-based single crystal superalloy, *J. Alloys Compd.* 724 (2017) 287-295.
- [17] Y. Tang, M. Huang, J. Xiong, J. Li, J. Zhu, Evolution of superdislocation structures during tertiary creep of a nickel-based single-crystal superalloy at high temperature and low stress, *Acta Mater.* 126 (2017) 336-345.
- [18] S. Yamasaki, M. Mitsuhashi, H. Nakashima, Deformation Microstructure and Fracture Behavior in Creep-Exposed Alloy 617, *Mater. Trans.* 58(3) (2017) 442-449.
- [19] L. Cui, J. Yu, J. Liu, T. Jin, X. Sun, The creep deformation mechanisms of a newly designed nickel-base superalloy, *Mater. Sci. Eng. A* 710 (2018) 309-317.
- [20] D. Qi, D. Wang, K. Du, Y. Qi, L. Lou, J. Zhang, H. Ye, Creep deformation of a nickel-based single crystal superalloy under high stress at 1033 K, *J. Alloys Compd.* 735 (2018) 813-820.
- [21] J.J. Moverare, S. Johansson, R.C. Reed, Deformation and damage mechanisms during thermal-mechanical fatigue of a single-crystal superalloy, *Acta Mater.* 57(7) (2009) 2266-2276.
- [22] H.U. Hong, J.G. Kang, B.G. Choi, I.S. Kim, Y.S. Yoo, C.Y. Jo, A comparative study on thermomechanical and low cycle fatigue failures of a single crystal nickel-based superalloy, *Int. J. Fatigue* 33(12) (2011) 1592-1599.
- [23] H.U. Hong, B.G. Choi, I.S. Kim, Y.S. Yoo, C.Y. Jo, Characterization of deformation mechanisms during low cycle fatigue of a single crystal nickel-based superalloy, *J. Mater. Sci.* 46(15) (2011) 5245-5251.
- [24] A. Hynnä, V.-T. Kuokkala, J. Laurila, P. Kettunen, High-temperature low-cycle fatigue behavior of superalloy MA 760, *J. Mater. Eng. Perform.* 2(4) (1993) 531-535.
- [25] K.B. Sankara Rao, M.G. Castelli, G.P. Allen, J.R. Ellis, A critical assessment of the mechanistic aspects in HAYNES 188 during low-cycle fatigue in the range 25 °C to 1000 °C, *Metall. Mater. Trans. A* 28(2) (1997) 347-361.
- [26] B.S. Rho, S.W. Nam, X. Xie, The effect of test temperature on the intergranular cracking of Nb-A286 alloy in low cycle fatigue, *J. Mater. Sci.* 37(1) (2002) 203-209.



- [27] K. Kakehi, Influence of crystallographic orientation and stress waveforms on fatigue strength of single crystals of a Ni-base superalloy, *J. Jpn. Inst. Met.* 62(7) (1998) 653-661.
- [28] M. Nazmy, J. Denk, R. Baumann, A. Künzler, Environmental effects on tensile and low cycle fatigue behavior of single crystal nickel base superalloys, *Scr. Mater.* 48(5) (2003) 519-524.
- [29] I.S. Kim, B.G. Choi, J.E. Jung, J. Do, C.Y. Jo, Effect of microstructural characteristics on the low cycle fatigue behaviors of cast Ni-base superalloys, *Mater. Charact.* 106 (2015) 375-381.
- [30] X. Ma, H.J. Shi, J. Gu, Z. Yang, G. Chen, O. Luesebrink, H. Harders, Influence of surface recrystallization on the low cycle fatigue behaviour of a single crystal superalloy, *Fatigue Fract. Eng. Mater. Struct.* 38(3) (2015) 340-351.
- [31] S. Steuer, P. Villechaise, T.M. Pollock, J. Cormier, Benefits of high gradient solidification for creep and low cycle fatigue of AM1 single crystal superalloy, *Mater. Sci. Eng. A* 645 (2015) 109-115.
- [32] A. Bhattacharyya, G.V.S. Sastry, V.V. Kutumbarao, The origin of microtwinning at low strains during low-cycle fatigue of Inconel 718 at room temperature, *J. Mater. Sci.* 34(3) (1999) 587-591.
- [33] B.S. Rho, S.W. Nam, The effect of applied strain range on the fatigue cracking in Nb-A286 iron-base superalloy, *Mater. Lett.* 48(1) (2001) 49-55.
- [34] K.O. Findley, A. Saxena, Low cycle fatigue in rene 88DT at 650 °C: Crack nucleation mechanisms and modeling, *Metall. Mater. Trans. A* 37(5) (2006) 1469-1475.
- [35] M. Reger, L. Remy, High temperature, low cycle fatigue of IN-100 superalloy I: Influence of temperature on the low cycle fatigue behaviour, *Mater. Sci. Eng. A* 101 (1988) 47-54.
- [36] A. Shyam, W.W. Milligan, Effects of deformation behavior on fatigue fracture surface morphology in a nickel-base superalloy, *Acta Mater.* 52(6) (2004) 1503-1513.
- [37] D. Ye, Effect of cyclic straining at elevated-temperature on static mechanical properties, microstructures and fracture behavior of nickel-based superalloy GH4145/SQ, *Int. J. Fatigue* 27(9) (2005) 1102-1114.
- [38] S.G. Hong, S.B. Lee, T.S. Byun, Temperature effect on the low-cycle fatigue behavior of type 316L stainless steel: Cyclic non-stabilization and an invariable fatigue parameter, *Mater. Sci. Eng. A* 457(1) (2007) 139-147.
- [39] A. Pineau, S.D. Antolovich, High temperature fatigue of nickel-base superalloys – A review with special emphasis on deformation modes and oxidation, *Eng. Fail. Anal.* 16(8) (2009) 2668-2697.
- [40] J. Yu, X. Sun, T. Jin, N. Zhao, H. Guan, Z. Hu, High temperature creep and low cycle fatigue of a nickel-base superalloy, *Mater. Sci. Eng. A* 527(9) (2010) 2379-2389.
- [41] H.Y. Qin, G. Chen, Q. Zhu, C.J. Wang, P. Zhang, High Temperature Low Cycle Fatigue Behavior of GH4742 Alloy, *J. Iron Steel Res. Int.* 22(6) (2015) 551-556.
- [42] Z. He, Y. Zhang, W. Qiu, H.J. Shi, J. Gu, Temperature effect on the low cycle fatigue behavior of a directionally solidified nickel-base superalloy, *Mater. Sci. Eng. A* 676(Supplement C) (2016) 246-252.
- [43] Z. Chu, Y. Jinjiang, S. Xiaofeng, G. Hengrong, H. Zhuangqi, High temperature low cycle fatigue behavior of a directionally solidified Ni-base superalloy DZ951, *Mater. Sci. Eng. A* 488(1-2) (2008) 389-397.
- [44] R. Dewa, S. Kim, W. Kim, E. Kim, Effect of Strain Range on the Low Cycle Fatigue in Alloy 617 at High Temperature, *Metals* 7(2) (2017) 54.
- [45] M. Sundararaman, W. Chen, R.P. Wahi, A. Wiedenmann, W. Wagner, W. Petry, TEM and SANS investigation of age hardened nimonic PE16 after cyclic loading at room temperature, *Acta Metall. Mater.* 40(5) (1992) 1023-1028.
- [46] P. Li, Q.Q. Li, T. Jin, Y.Z. Zhou, J.G. Li, X.F. Sun, Z.F. Zhang, Comparison of low-cycle fatigue

- behaviors between two nickel-based single-crystal superalloys, *Int. J. Fatigue* 63 (2014) 137-144.
- [47] J.X. Zhang, J.C. Wang, H. Harada, Y. Koizumi, The effect of lattice misfit on the dislocation motion in superalloys during high-temperature low-stress creep, *Acta Mater.* 53(17) (2005) 4623-4633.
- [48] P. Li, Q.Q. Li, T. Jin, Y.Z. Zhou, J.G. Li, X.F. Sun, Z.F. Zhang, Effect of Re on low-cycle fatigue behaviors of Ni-based single-crystal superalloys at 900°C, *Mater. Sci. Eng. A* 603 (2014) 84-92.
- [49] L. Liu, J. Meng, J. Liu, T. Jin, X. Sun, H. Zhang, Effects of crystal orientations on the cyclic deformation behavior in the low cycle fatigue of a single crystal nickel-base superalloy, *Mater. Des.* 131 (2017) 441-449.
- [50] S.D. Antolovich, S. Liu, R. Baur, Low cycle fatigue behavior of René 80 at elevated temperature, *Metall. Trans. A* 12(3) (1981) 473-481.
- [51] P.J. Phillips, R.R. Unocic, L. Kovarik, D. Mourer, D. Wei, M.J. Mills, Low cycle fatigue of a Ni-based superalloy: Non-planar deformation, *Scr. Mater.* 62(10) (2010) 790-793.
- [52] R. Chieragatti, L. Remy, Influence of orientation on the low cycle fatigue of MAR-M 200 single crystals at 650 °C II: Cyclic stress-strain behaviour, *Mater. Sci. Eng. A* 141(1) (1991) 11-22.
- [53] L. Cui, H. Su, J. Yu, J. Liu, T. Jin, X. Sun, Temperature dependence of tensile properties and deformation behaviors of nickel-base superalloy M951G, *Mater. Sci. Eng. A* 696 (2017) 323-330.
- [54] G. Liu, J. Salvat Cantó, S. Winwood, K. Rhodes, S. Biroasca, The effects of microstructure and microtexture generated during solidification on deformation micromechanism in IN713C nickel-based superalloy, *Acta Mater.* 148 (2018) 391-406.
- [55] G. Liu, S. Winwood, K. Rhodes, S. Biroasca, The effects of grain size, dendritic structure and crystallographic orientation on fatigue crack propagation in IN713C nickel-based superalloy, *Int. J. Plast* 125 (2020) 150-168.
- [56] F.O. Riemelmoser, R. Pippan, H.P. Stüwe, An argument for a cycle-by-cycle propagation of fatigue cracks at small stress intensity ranges, *Acta Mater.* 46(5) (1998) 1793-1799.
- [57] H. Cai, A.J. McEvily, On striations and fatigue crack growth in 1018 steel, *Mater. Sci. Eng. A* 314(1) (2001) 86-89.
- [58] L. Cui, H. Su, J. Yu, J. Liu, T. Jin, X. Sun, The creep deformation and fracture behaviors of nickel-base superalloy M951G at 900 degrees C, *Mater. Sci. Eng. A* 707 (2017) 383-391.
- [59] G. Wang, Y. Sun, X. Wang, J. Liu, J. Liu, J. Li, J. Yu, Y. Zhou, T. Jin, X. Sun, X. Sun, Microstructure evolution and mechanical behavior of Ni-based single crystal superalloy joint brazed with mixed powder at elevated temperature, *Journal of Materials Science & Technology* 33(10) (2017) 1219-1226.
- [60] J. Reuchet, L. Remy, High temperature low cycle fatigue of MAR-M 509 superalloy I: The influence of temperature on the low cycle fatigue behaviour from 20 to 1100°C, *Materials Science and Engineering* 58(1) (1983) 19-32.
- [61] L. Zheng, M. Zhang, R. Chellali, J. Dong, Investigations on the growing, cracking and spalling of oxides scales of powder metallurgy Rene95 nickel-based superalloy, *Appl. Surf. Sci.* 257(23) (2011) 9762-9767.
- [62] L. Viskari, M. Hörnqvist, K.L. Moore, Y. Cao, K. Stiller, Intergranular crack tip oxidation in a Ni-base superalloy, *Acta Mater.* 61(10) (2013) 3630-3639.
- [63] L.Z. He, Q. Zheng, X.F. Sun, H.R. Guan, Z.Q. Hu, A.K. Tieu, C. Lu, H.T. Zhu, High temperature low cycle fatigue behavior of Ni-base superalloy M963, *Mater. Sci. Eng. A* 402(1-2) (2005) 33-41.
- [64] P. Kontis, E. Alabort, D. Barba, D.M. Collins, A.J. Wilkinson, R.C. Reed, On the role of boron on improving ductility in a new polycrystalline superalloy, *Acta Mater.* 124 (2017) 489-500.
- [65] P. Kontis, D.M. Collins, A.J. Wilkinson, R.C. Reed, D. Raabe, B. Gault, Microstructural degradation

- of polycrystalline superalloys from oxidized carbides and implications on crack initiation, *Scr. Mater.* 147 (2018) 59-63.
- [66] M. Maldini, M. Marchionni, M. Nazmy, M. Staubli, G. Osinkolu, Creep and fatigue properties of a directionally solidified nickel base superalloy at elevated temperature, TMS, Warrendale, PA, USA, (1996) 327-334.
- [67] H. Mughrabi, S. Kraft, M. Ott, Specific aspects of isothermal and anisothermal fatigue of the monocrystalline nickel-base superalloy CMSX-6, TMS, Warrendale, PA, USA (1996) 135.
- [68] M. Ott, H. Mughrabi, Dependence of the high-temperature low-cycle fatigue behaviour of the monocrystalline nickel-base superalloys CMSX-4 and CMSX-6 on the  $\gamma/\gamma'$ -morphology, *Mater. Sci. Eng. A* 272(1) (1999) 24-30.
- [69] B. Lerch, V. Gerold, Room temperature deformation mechanisms in Nimonic 80A, *Acta Metall.* 33(9) (1985) 1709-1716.
- [70] B.A. Lerch, V. Gerold, Cyclic hardening mechanisms in NIMONIC 80A, *Metall. Trans. A* 18(12) (1987) 2135-2141.
- [71] M. Valsan, P. Parameswaran, K. Bhanu Sankara Rao, M. Vijayalakshmi, S.L. Mannan, D.H. Shastry, High-temperature low-cycle fatigue behavior of a NIMONIC PE-16 superalloy—Correlation with deformation and fracture, *Metall. Trans. A* 23(6) (1992) 1751-1761.
- [72] S. Ganesh Sundara Raman, K.A. Padmanabhan, Room-temperature low-cycle fatigue behaviour of a Ni-base superalloy, *Int. J. Fatigue* 16(3) (1994) 209-215.
- [73] J.K. Wright, L.J. Carroll, C. Cabot, T.M. Lillo, J.K. Benz, J.A. Simpson, W.R. Lloyd, J.A. Chapman, R.N. Wright, Characterization of elevated temperature properties of heat exchanger and steam generator alloys, *Nucl. Eng. Des.* 251 (2012) 252-260.
- [74] J.K. Wright, L.J. Carroll, J.A. Simpson, R.N. Wright, Low Cycle Fatigue of Alloy 617 at 850 °C and 950 °C, *J. Eng. Mater. Technol.* 135(3) (2013).
- [75] S. Guan, C. Cui, Y. Yuan, Y. Gu, The role of phosphorus in a newly developed Ni-Fe-Cr-based wrought superalloy, *Mater. Sci. Eng. A* 662 (2016) 275-282.
- [76] K. Dong, C. Yuan, S. Gao, C. Jia, J. Guo, C. Ge, Creep properties of a powder metallurgy disk superalloy at 700 °C, *J. Mater. Res.* (2017) 1-10.
- [77] T.P. Gabb, G. Welsch, The high temperature deformation in cyclic loading of a single crystal nickel-base superalloy, *Acta Metall.* 37(9) (1989) 2507-2516.
- [78] I.M. Lifshitz, V.V. Slyozov, The kinetics of precipitation from supersaturated solid solutions, *J. Phys. Chem. Solids* 19(1) (1961) 35-50.
- [79] C. Wagner, Theorie der alterung von niederschlägen durch umlosen (Ostwald-Reifung), *Z. Elektrochem.* 65(7-8) (1961) 581-591.
- [80] M.R. Daymond, M. Preuss, B. Clausen, Evidence of variation in slip mode in a polycrystalline nickel-base superalloy with change in temperature from neutron diffraction strain measurements, *Acta Mater.* 55(9) (2007) 3089-3102.
- [81] P. Li, S.X. Li, Z.G. Wang, Z.F. Zhang, Fundamental factors on formation mechanism of dislocation arrangements in cyclically deformed fcc single crystals, *Prog. Mater. Sci.* 56(3) (2011) 328-377.
- [82] Q. Jiang, D.S. Zhao, M. Zhao, Size-dependent interface energy and related interface stress, *Acta Mater.* 49(16) (2001) 3143-3147.
- [83] T. Murakumo, T. Kobayashi, Y. Koizumi, H. Harada, Creep behaviour of Ni-base single-crystal superalloys with various  $\gamma'$  volume fraction, *Acta Mater.* 52(12) (2004) 3737-3744.